Remote Sens. **2009**, *1*, 300-317; doi:10.3390/rs1030300

OPEN ACCESS

Remote Sensing

ISSN 2072-4292

www.mdpi.com/journal/remotesensing

Article

Numerical Simulation of the Full-Polarimetric Emissivity of Vines and Comparison with Experimental Data

Alberto Martinez-Vazquez [1,*], Adriano Camps [1,2], Juan Manuel Lopez-Sanchez [3], Mercedes Vall-llossera [1,2] and Alessandra Monerris [1,2]

[1] Remote Sensing Laboratory, Dept. Teoria del Senyal i Comunicacions, Universitat Politècnica de Catalunya, Campus Nord - D3, Jordi Girona 1-3, E-08034 Barcelona, Spain; E-Mails: camps@tsc.upc.edu (A.C.); merce@tsc.upc.edu (M.V.); sandra.monerris@tsc.upc.edu (A.M.)

[2] SMOS Barcelona Expert Centre, Pg. Marítim de la Barceloneta 37-49, E-08003, Barcelona, Spain

[3] Dept. Physics, System Engineering and Signal Theory, University of Alicante, P.O.Box 99, E-03080 Alicante, Spain; E-Mail: juanma.lopez@ua.es

* Author to whom correspondence should be addressed; E-Mail: alberto2kmv-upc@yahoo.es; Tel.: +34-934-054-153; Fax: +34-934-017-232

Received: 30 April 2009; in revised form: 2 July 2009 / Accepted: 11 July 2009 / Published: 20 July 2009

Abstract: Surface soil moisture is a key variable needed to understand and predict the climate. L-band microwave radiometry seems to be the best technique to remotely measure the soil moisture content, since the influence of other effects such as surface roughness and vegetation is comparatively small. This work describes a numerical model developed to efficiently compute the four elements of the Stokes emission vector (T_h, T_v, T_U and T_V) of vegetation-covered soils at low microwave frequencies, as well as the single-scattering albedo and the extinction coefficient of the vegetation layer over a wide range of incidence angles. A comparison with L-band (1.400–1.427 MHz) experimental radiometric data gathered during the SMOS REFLEX 2003 field experiment over vines is presented and discussed. The measured and simulated emissivities at vertical polarization agree very well. However, at horizontal polarization there is some disagreement introduced by the soil emission model. Important radiometric parameters, such as the albedo, the attenuation and the transmissivity are computed and analyzed in terms of their values and trends, as well as their dependence on the observation and scene parameters. It is found that the vegetation attenuation is mainly driven by the presence of branches and leaves, while the albedo is

mainly driven by the branches. The comparison of the simulated parameters with the values obtained by fitting the experimental data with the τ-ω model is very satisfactory.

Keywords: polarimetric radiometry; Stokes parameters; emission; scattering; vegetation; vines; L-systems; soil moisture

1. Introduction

In May 1999 the SMOS Earth Explorer Opportunity mission [1,2] was selected by ESA to provide global soil moisture and sea salinity maps which are key variables in weather, climate and extreme event forecasts. As a secondary objective, data acquired over ice/snow regions may be used to indicate climate changes due to the greenhouse effect. SMOS' single payload is MIRAS, an innovative 2-D L-band aperture synthesis interferometric radiometer that will be able to measure the full modified Stokes emission vector from a wide 2-D field of view (swath ~800 km, incidence angles from 0° to ~60°). An important feature of this instrument is that, as the satellite moves along its track, a collection of brightness temperatures emitted from the same area on the Earth will be observed under a large range of incidence angles. As a result, the variation of the emissivity as a function of the incidence angle can be exploited in the retrieval of soil moisture and vegetation parameters. This new capability predicts better results than those obtained with other existing radiometers that scan the surface at a single incidence angle. However, as in any inversion problem in geophysical sciences and engineering, the retrieval of soil moisture relies on the accuracy of both the forward emission models (vegetation description and numerical emission model) used to develop the inversion procedure over the range of observed incidence angles, and on the quality of the auxiliary data [3]. To improve these models, a number of field experiments have been conducted both over land and over sea [4]. In the case we are dealing with, the vegetation and soil layers must be modeled together to develop an accurate forward model. Models reported in the literature provide the first two modified Stokes emission elements (T_v, T_h) as a function of frequency and biophysical parameters of soil and vegetation, but not -to our knowledge- the third and fourth modified Stokes elements (T_U and T_V).

In this work a numerical model is presented to efficiently compute the complete modified Stokes emission vector (T_v, T_h, T_U and T_V) of vegetation-covered soils at low microwave frequencies over a wide range of incidence angles, as required for future retrieval algorithms suitable to the SMOS mission. Simulations have been compared to SMOS REFLEX 2003 radiometric data and to the retrieved vegetation opacity and albedo estimated using the τ-ω model as forward model in the minimization algorithm [5]. This comparison gives a clue on the confidence of both models (the complete electromagnetic model and the simplified τ-ω model) to describe the emissivity of vegetation-covered soils and helps pointing out their weaknesses.

The text is organized as follows. Section 2 reviews the basic concepts on emission theory. Sections 3 and 4 describe the possibilities for modeling the scenario of a vegetation-covered soil from the geometric and electromagnetic points of view, respectively. Finally, Section 5 presents the inter-comparison of simulation results modeling the scenario of the SMOS REFLEX 2003 field experiment

and the experimental data, including the variation of the emissivity, single-scattering albedo and extinction with the incidence angle.

2. Basic Concepts on Emission Theory

The modified Stokes emission vector $\bar{e}(\theta,\phi) = [e_v\ e_h\ e_U\ e_V]^T$ is related to the electric fields incident in the antenna at vertical and horizontal polarizations (E_v and E_h [V/m]) by [6; pp. 24-25]:

$$\begin{bmatrix} T_v(\theta,\phi) \\ T_h(\theta,\phi) \\ T_U(\theta,\phi) \\ T_V(\theta,\phi) \end{bmatrix} = T_s \begin{bmatrix} e_v(\theta,\phi) \\ e_h(\theta,\phi) \\ e_U(\theta,\phi) \\ e_V(\theta,\phi) \end{bmatrix} = \frac{\lambda^2}{\eta\ k_B\ B} \begin{bmatrix} \langle E_v E_v^* \rangle \\ \langle E_h E_h^* \rangle \\ 2\,\mathrm{Re}\langle E_v E_h^* \rangle \\ 2\,\mathrm{Im}\langle E_v E_h^* \rangle \end{bmatrix} \tag{1}$$

where:

- T_v and T_h are brightness temperatures at vertical and horizontal polarizations, respectively,
- T_U and T_V are the third and fourth modified Stokes elements, respectively,
- T_s is the surface's soil temperature (assumed to be constant with depth),
- λ is the electromagnetic wavelength, η is the wave impedance, k_B is the Boltzmann's constant, B is the radiometer's noise bandwidth, and
- $< >$ stands for the expectation operator.

The problem of computing the modified Stokes emission vector of a vegetation-covered soil is very complex. To the moment, two approaches have been proposed to solve it: those based on an incoherent approach by using the τ-ω model, and those based on a coherent approach by using the Radiative Transfer Equation (RTE) with the discrete definition of the vegetation components and the interaction among them. The simulator presented in this manuscript falls into the second group, although some simplifications applicable at L-band have been considered in order to keep the simulation time under a reasonable limit (~1 h) on a mid-range personal computer. Further information on these models is given in the next sections.

2.1. The Simplified τ-ω Model

For the L-band it is usually assumed that scattering effects are much smaller than absorption effects, that the single scattering is dominant, takes place in the forward direction, and that the vegetation and soil temperatures are equal (Figure 1). As a result, the equation widely used in microwave radiometry is the simple τ-ω model [7]:

$$e_{h,v} = \left(1 + \frac{\Gamma_{h,v}^{soil}}{L_{h,v}^{canopy}}\right)\left(1 - \frac{1}{L_{h,v}^{canopy}}\right)\left(1 - \omega_{h,v}^{canopy}\right) + \frac{1 - \Gamma_{h,v}^{soil}}{L_{h,v}^{canopy}} \tag{2}$$

and $e_{U,V} = 0$. The τ-ω model takes into account both the soil emission $e_{h,v}^{soil} = 1 - \Gamma_{h,v}^{soil}$ [second term in Equation (2)], and the vegetation emission. In Equation (1) $\Gamma_{v,h}^{soil} \triangleq [(1-Q)\cdot\Gamma_{v,h}^{specular} + Q\cdot\Gamma_{h,v}^{specular}]e^{-hs\cdot\cos\theta}$, being Q the polarization mixing factor, $\Gamma_{h,v}^{specular}$ the Fresnel reflection coefficient, and hs a parameter that

accounts for surface roughness effects [7]. In Equation (2) the vegetation layer attenuation is estimated as:

$$L_{v,h}^{canopy} = e^{\tau_{v,h}} \tag{3}$$

where τ_p is the opacity of the vegetation layer of thinkness *hly*:

$$\begin{aligned} \tau_v &= \int_0^{hly} k_{e11}(\theta,\phi)ds \\ \tau_h &= \int_0^{hly} k_{e22}(\theta,\phi)ds \end{aligned} \tag{4}$$

and k_{e11} and k_{e22} are the extinction coefficients at *v* and *h* polarizations, elements 11 and 22 of the extinction matrix $\overline{\overline{k_e}}$ [8, p. 274]:

$$\overline{\overline{k_e}} = \frac{2\pi\, n_0}{k}\begin{bmatrix} 2\,\mathrm{Im}(f_{vv}) & 0 & \mathrm{Im}(f_{vh}) & -\mathrm{Re}(f_{vh}) \\ 0 & 2\,\mathrm{Im}(f_{hh}) & \mathrm{Im}(f_{hv}) & \mathrm{Re}(f_{hv}) \\ 2\,\mathrm{Im}(f_{hv}) & 2\,\mathrm{Im}(f_{vh}) & \mathrm{Im}(f_{vv}+f_{hh}) & \mathrm{Re}(f_{vv}-f_{hh}) \\ 2\,\mathrm{Re}(f_{hv}) & -2\,\mathrm{Re}(f_{vh}) & \mathrm{Re}(f_{hh}-f_{vv}) & \mathrm{Im}(f_{vv}+f_{hh}) \end{bmatrix} \tag{5}$$

being n_0 the number of particles per unit of volume (n_0 is equal to the ratio of number of scatterers over the product of the antenna footprint by the depth of the layer in which the vegetation has been divided), *k* the wave number, and f_{pq} the forward scattering amplitudes, which are computed as the sum of the forward scattering amplitudes of each individual scatterer (branches, leaves, ...).

The single-scattering albedo $\omega_{h,v}^{canopy}$ can be computed as:

$$\begin{aligned} \omega_v^{canopy} &= \frac{\int\left[P_{11}(\theta,\phi,\theta',\phi') + P_{21}(\theta,\phi,\theta',\phi')\right]d\Omega'}{k_{e11}(\theta,\phi)} \\ \omega_h^{canopy} &= \frac{\int\left[P_{12}(\theta,\phi,\theta',\phi') + P_{22}(\theta,\phi,\theta',\phi')\right]d\Omega'}{k_{e22}(\theta,\phi)} \end{aligned} \tag{6}$$

where P_{11}, P_{21}, P_{12} and P_{22} are 11, 21, 12 and 22 elements of the phase matrix $\overline{\overline{P}}(\theta,\theta',\phi,\phi')$ [8, pp. 126 and 271]:

$$\overline{\overline{P}}(\theta,\theta',\phi,\phi') = n_0\begin{bmatrix} |f_{vv}|^2 & |f_{vh}|^2 & \mathrm{Re}(f_{vh}^* f_{vv}) & -\mathrm{Im}(f_{vh}^* f_{vv}) \\ |f_{hv}|^2 & |f_{hh}|^2 & \mathrm{Re}(f_{hh}^* f_{hv}) & -\mathrm{Im}(f_{hh}^* f_{hv}) \\ 2\,\mathrm{Re}(f_{vv} f_{hv}^*) & 2\,\mathrm{Re}(f_{vh} f_{hh}^*) & \mathrm{Re}(f_{vv} f_{hh}^* + f_{vh} f_{hv}^*) & -\mathrm{Im}(f_{vv} f_{hh}^* - f_{vh} f_{hv}^*) \\ 2\,\mathrm{Im}(f_{vv} f_{hv}^*) & 2\,\mathrm{Im}(f_{vh} f_{hh}^*) & \mathrm{Im}(f_{vv} f_{hh}^* + f_{vh} f_{hv}^*) & \mathrm{Re}(f_{vv} f_{hh}^* - f_{vh} f_{hv}^*) \end{bmatrix} \tag{7}$$

In Equations (5) and (7) the f_{pq} coefficients are the vector-scattering amplitude functions that provide the amplitude, phase and polarization information of the scattered field at *q*-polarization $\vec{E}_q = \hat{e}_q f_{pq}(\theta,\theta',\phi,\phi')e^{-jkr}/r$, when a plane wave at *p*-polarization $\vec{E}_i = \hat{e}_p e^{-j\vec{k}_{inc}\vec{r}}$ is incident on each scatterer. Note that this expression assumes a far-field situation, so the interaction between near particles is implicitly neglected in the model. The impact of this assumption will be revised in Section 5.

At L-band, up to moderate-high incidence angles it is usually assumed that $\tau_p(\theta) = \tau_p(0)/\cos\theta$, and that ω_p^{canopy} is independent of the incidence angle. For vegetation layers without a dominant

vertical or horizontal structure it is also very common to assume that these quantities are polarization independent.

The goodness of the τ-ω model [Equation (2)] was checked by [5] by fitting the model parameters (τ and ω) using L-band radiometric data up to 50° incidence angle acquired over a vineyard in the Valencia Anchor Station. This site has already been selected as a SMOS cal/val site. In the following sections the emissivities, and τ and ω values predicted using the electromagnetic model described in this study will be compared to the measured emissivities and the estimated τ-ω values in [5].

Figure 1. Soil + vegetation configuration in the τ-ω model.

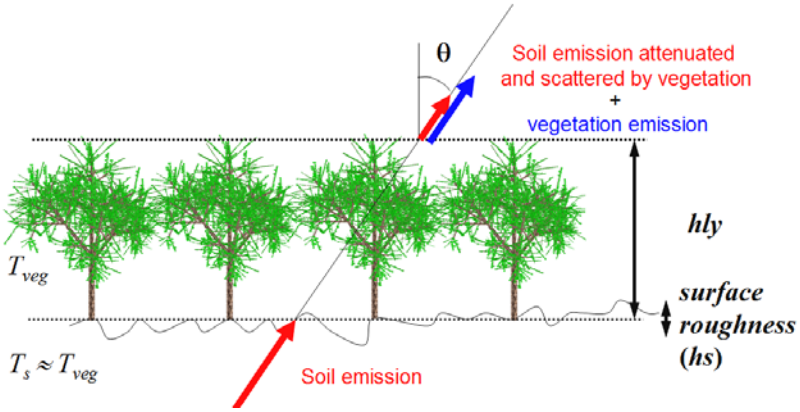

2.2. The Complete Polarimetric Radiative Transfer Equation (RTE)

The polarimetric emission can be computed by means of the RTE [8, pp. 281-282] as:

$$\frac{d\bar{e}(\theta,\phi)}{ds} = -\bar{\bar{k}}_e(\theta,\phi)\,\bar{e}(\theta,\phi) + \bar{F}(\theta,\phi) + \int_0^{2\pi}\int_0^{\pi} \bar{\bar{P}}(\theta,\phi,\theta',\phi')\bar{e}(\theta,\phi)d\Omega' \tag{8}$$

The emission vector $\bar{F}(\theta,\phi)$ in Equation (6) is given by [8, p. 282]:

$$\begin{aligned}
&\bar{F}(\theta,\phi) = [k_{a1}(\pi-\theta,\pi+\phi)\;\; k_{a2}(\pi-\theta,\pi+\phi)\;\; -k_{a3}(\pi-\theta,\pi+\phi)\;\; -k_{a4}(\pi-\theta,\pi+\phi)]^T \\
&k_{a1}(\theta,\phi) = k_{e11}(\theta,\phi) - \int\left[P_{11}(\theta,\phi,\theta',\phi') + P_{21}(\theta,\phi,\theta',\phi')\right]d\Omega' \\
&k_{a2}(\theta,\phi) = k_{e22}(\theta,\phi) - \int\left[P_{12}(\theta,\phi,\theta',\phi') + P_{22}(\theta,\phi,\theta',\phi')\right]d\Omega' \\
&k_{a3}(\theta,\phi) = 2k_{e13}(\theta,\phi) + 2k_{e23}(\theta,\phi) - 2\int\left[P_{13}(\theta,\phi,\theta',\phi') + P_{23}(\theta,\phi,\theta',\phi')\right]d\Omega' \\
&k_{a4}(\theta,\phi) = -2k_{e14}(\theta,\phi) - 2k_{24}(\theta,\phi) + 2\int\left[P_{14}(\theta,\phi,\theta',\phi') + P_{24}(\theta,\phi,\theta',\phi')\right]d\Omega'.
\end{aligned} \tag{9}$$

Next, the solution of Equation (8) entails the application of the following boundary conditions:

- $\bar{T}_{up,p}(\theta,\phi,z=0)$ the soil surface emission, and
- $\bar{T}_{dn,p}(\theta,\phi,z=h)$ the downwelling atmospheric emission at the top of the vegetation layer.

At L-band, since the soil emission ($T_{up,v}$ and $T_{up,h}$) and the vegetation emission are much larger (about two orders of magnitude) than the atmospheric downwelling contributions, as a first approximation $\bar{T}_{dn,p}(\theta,\phi,z=h)$ could be neglected at nadir. Nevertheless, since different elevation angles are considered in the analysis performed in Section 5, both the atmospheric downwelling contribution and the cosmic background (≈ 2.1 K + 2.7 K = 4.8 K at zenith) have been accounted for

(the Galactic contribution has been ignored in the model), and corrected by the secant of the elevation angle, which is a good approximation up to the maximum incidence angles we are dealing with.

It should be noted that in the computation of the phase matrix [Equation (7)] the interaction between the vegetation elements and the soil has been considered up to first order, as described in [9]. This includes: a) the direct scattered field, b) the scattered field when the incident field is reflected on the soil, c) the scattered field reflected on the soil when the incident field impinges directly to the element, and d) the combination of b) and c) (Figure 2). This assumption together with the far-field simplification helps to maintain the overall computation complexity at an affordable level.

Figure 2. Four contributions to the scattered fields considered in the model. From left to right: trunk-trunk, trunk-ground, ground-trunk, and ground-truck-ground.

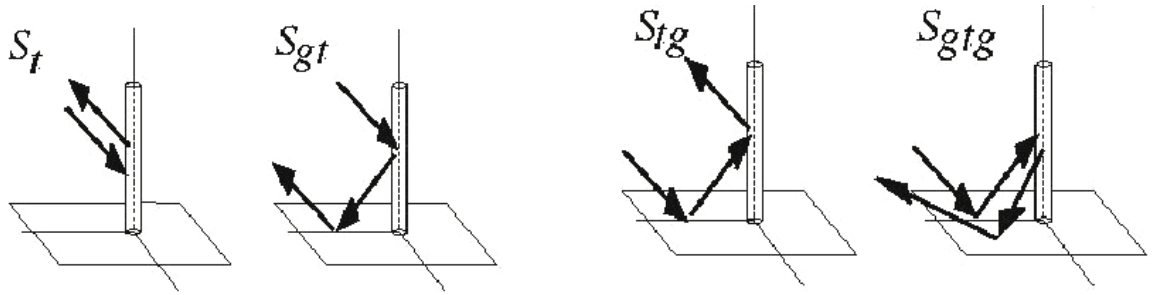

3. Geometric Description of the Scenario

The simulator models the scenario under study as a rough terrain and a vegetation layer occupying the footprint of the radiometer's antenna (Figure 3). To account for different spatial distributions of plants, the simulator allows random as well as uniform positioning of the plants over the field-of-view of the radiometer. Random distribution of the plants is used to model forested areas, whereas a uniform distribution is used for modeling man-made scenarios such as agricultural fields as the SMOS REFLEX 2,003 site.

Figure 3. Sample random tree distribution over a rough soil inside the antenna footprint (leaves not drawn).

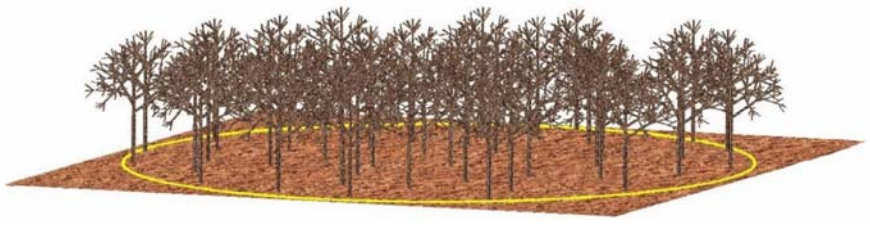

In order to simplify the radiometric simulations, the plant model is repeated within the illuminated area. In a natural scenario randomness is preserved since the phase associated with each random position in the illuminated area is random itself and, in addition, Monte-Carlo simulations with different plant positions are performed before the simulated emissivities are averaged. The validity of this approximation has been checked by comparing the results to those of a full simulation with different plants generated for each different position. The extremely high computation time of the

second option hampers to perform the analysis as a function of system and plants parameters. The geometric description of the different components used to model the scenario, with particular emphasis on the elements used to model the vines analyzed in Section 5, is presented hereafter.

3.1. Soil Surface

The terrain is modeled as a Gaussian rough surface characterized by its rms height (σ_h) and its correlation lengths $l_x = l_y = l$. A plowed terrain may present different correlation lengths in the *X* and *Y* directions, thus inducing an azimuthal effect on the Stokes elements, but this assumption has not been considered in this manuscript.

In addition, a constant slope can be considered in the simulator through the definition of the vector normal to the soil by its elevation and azimuth angles. For the vines analyzed in Section 5 no slope has been considered.

3.2. Trunks and Branches

The vegetation layer is modeled by a set of simple discrete scatterers for which an analytical formulation for the scattered fields exists. Trunks and branches are dielectric cylinders, optionally with an external corrugation, which are arranged following a fractal geometry described by Lindenmayer systems (L-systems) [10]. An iterative method and rules describing the growth from the tree trunk to the branches, is schematically shown in Figure 4a. Figure 4b shows a detail of the leaves in a terminal branch. Figure 4c,d present a sample of cereals and rice, respectively. Finally, Figure 4e,f,g show examples of the final stage of other types of plants generated with a fractal geometry. Each element in the plant is characterized by its center position in the tree reference frame ($\vec{r}_j$), its orientation ($\vec{k}_j$), its length (L_j), and radius (R_j). Similarly, each plant is characterized by its point of birth over the field of view ($\vec{r}_{kTrunk}$), hence having for each scatterer the absolute position in the global frame of the illuminated area.

The particular model used for a vine is shown in Figure 5b, including leaves, and an external corrugation to model the roughness of the trunk and branches. Figure 6a shows the histogram of the elevation angle of the branches used in the vine model, weighted by the volume of each element. Apart from the bar at 0 deg corresponding to the trunk, the rest of branches are distributed between 20 and 95 deg.

3.3. Stems and Leaves

Once the structure of the trunk and branches has been defined by the L-system, the stems and leaves are added to the tree model (Figure 4b) using an algorithm based on the density of these elements so as to adjust the measured leaf area index (*LAI*) [11,12].

Stems, like branches, are modeled by dielectric cylinders, optionally with an external corrugation. They are positioned only over the final branches (branches with the higher fractal iteration order), and

are characterized also by its center position in the tree reference frame ($\vec{r}_j$), its orientation ($\vec{k}_j$), length (L_j), and radius (R_j).

Leaves are modeled as flattened ellipsoids in one dimension (disc: flat leave) or in two dimensions (needles). Leaves are positioned only over the stems and are characterized by its center position in the tree reference frame ($\vec{r}_j$), the orientation of their major axis ($\vec{k}_j$), and the radii of its semi-axes (R_{j1} and R_{j2}). Due to the extremely large number of leaves per plant, the set of possible sizes and orientations is discretized (3 possible sizes and $\Delta\theta = \Delta\phi = 22.5$). Therefore, only a finite set of scattering coefficients must be computed, and the total computation time remains acceptable (Computation time is about 20 minutes for the scenario presented in section 5 on a PC at 2,400 MHz with 1,024 Mbytes of RAM).

For the vine model of Figure 5b, each final branch has between 6 and 12 stems (uniformly randomly distributed), and each stem holds a number of leaves that covers all the stem length. Leaves are modeled as disks (flattened ellipsoids in one dimension). Figure 6b shows the histogram of the elevation angle of the stems used in the vine model, weighted by the volume of each element. They follow a distribution centered at 90 deg, since usually stems are grouped in couples, and less often in triplets, starting from a common node of the final branch. Figure 6c shows the histogram of the leaves elevation angle. The discretization in orientation explained previously can be clearly observed.

Figure 4. a) Iterative growing process of a tree, b) Detail of leaves in a terminal branch, c) Samples of cereals, d) Clusters of agricultural crops (e.g. rice), e) Sample bush, f) Sample palm tree, and g) Sample deciduous tree.

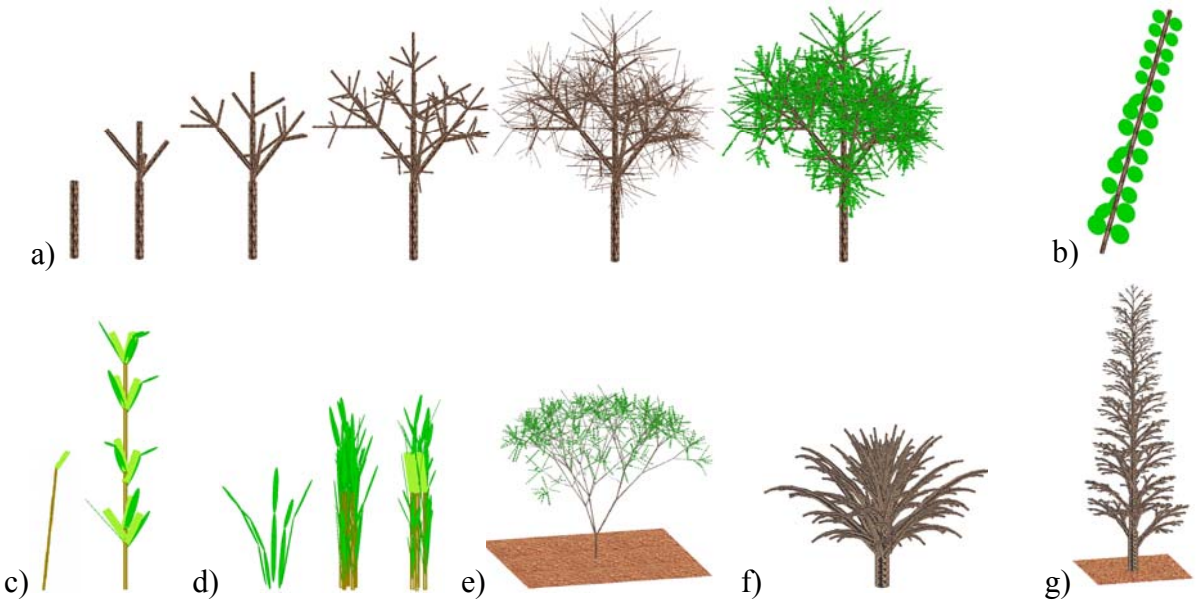

Figure 5. a) Picture of a vine at the SMOS REFLEX 2003 site, b) geometric model of a vine without the fruits, and c) vineyard scenario: vines are planted every 1.5 m in rows spaced 2.5 m.

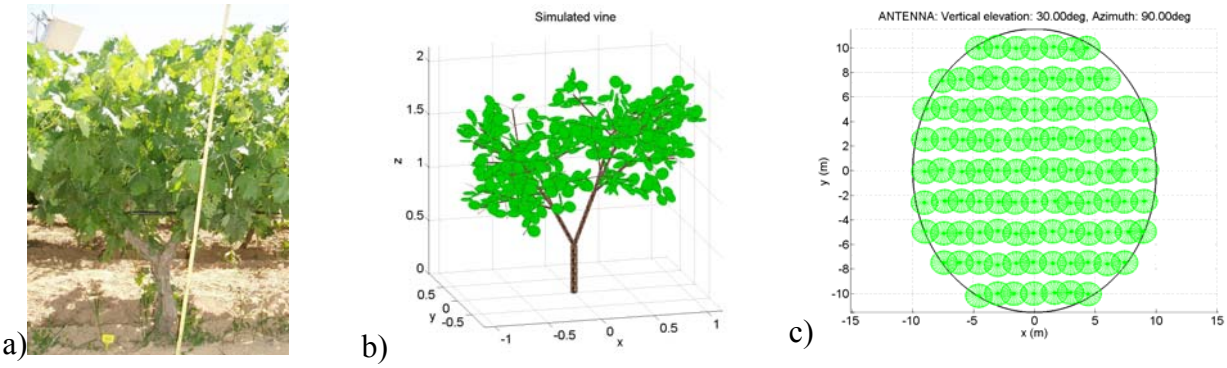

Figure 6. Histogram of the elevation angle of the vegetation elements weighted by the volume occupied a) Branches, b) stems, and c) Leaves.

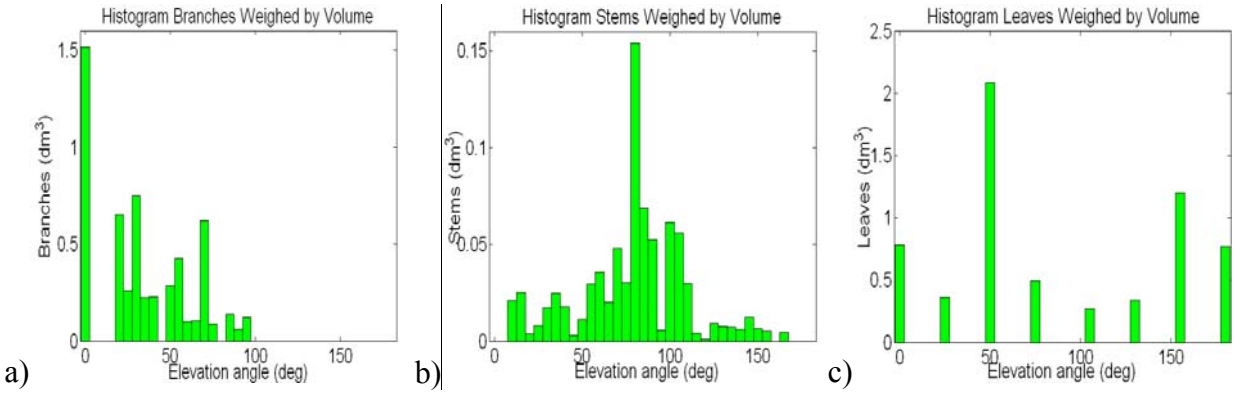

3.4. Fruits

Fruits are modeled as dielectric spheres of radius R uniformly distributed over the top part of the vegetation layer. In the context of the SMOS REFLEX 2003, the fruits are the grapes, and, in order to simplify the geometric and electromagnetic models, no clustering effects have been considered. Because of the typical high water content of these components, the number of fruits is determined from the volumetric water content (VWC) per plant [kg], the water fraction (WF) [dimensionless] of the fruits with respect to the whole plant, and the dry matter fraction (DMF) [dimensionless] of the fruits:

$$N_{fruits} = \frac{(VWC \cdot WF / d_{water})/(1 - DMF)}{4/3\pi R^3} \tag{10}$$

where $d_{water} = 1.01 \times 10^3$ kg/m^3 is the water density. Fruits are characterized by their center position in the tree reference frame ($\vec{r}_j$) and their radius (R_j).

4. Electromagnetic Description of the Scenario

In order to provide the maximum flexibility to the simulator, several scattering methods have been implemented, covering the different shapes and dimensions of the elements in the scenario.

4.1. Soil Surface

At horizontal and vertical polarizations the soil emission is efficiently computed using the expression by [13] considering the polarization mixing parameter Q and the rms height of the terrain. The Kirchhoff model [8, pp. 925-942] is also implemented in the simulator, with correlation lengths $l = l_x = l_y$, and the above mentioned parameters to compute the bistatic scattering coefficients of the terrain (σ^0_{pp} and σ^0_{pq} with $p, q = h$ or v). These coefficients, once integrated over the upper hemisphere using:

$$e_p(\theta,\varphi) = 1 - \frac{1}{4\pi\cos\theta}\iint_{2\pi}\left[\sigma^0_{pp}(\theta',\varphi',\theta,\varphi) + \sigma^0_{pq}(\theta',\varphi',\theta,\varphi)\right] d\Omega' \tag{11}$$

provide the full-polarimetric emissivity vector of the soil. In both cases, since the correlation length is the same in both directions, for a horizontal soil the third and fourth Stokes parameters are equal to zero ($e_U = e_V = 0$). If the soil surface had a certain slope or $l_x \neq l_y$, then $e_U \neq 0$, but $e_V = 0$. The effect of the volumetric soil moisture (W) is introduced in the model through the simple Wang soil dielectric permittivity model [14], or [15], or more complete models that take into account the soil texture and porosity [16].

4.2. Trunks, Branches and Stems

Two methods have been implemented for the computation of the scattering by trunks, branches and stems: the semiexact solution [17], and the physical optics solution for multilayer finite length cylinders with corrugation [18]. Based on the physical dimensions of the different components, one method or the other is chosen for the computation of the scattering matrix within the validity region of each method.

4.3. Leaves and Fruits

The scattering by leaves is computed using the Rayleigh-Gans approximation [17,19,20] for ellipsoids in its different particularizations for flat ellipses, flat discs and needles.

Fruits (grapes in the vine model) are modeled as dielectric spheres, so the Mie scattering formulation of a group of randomly distributed spherical scatterers has been implemented [8, pp. 352-362].

5. Comparison with Experimental Data from a Vineyard: SMOS REFLEX 2003 Field Experiment

The SMOS REFerence pixel L-band EXperiment (SMOS REFLEX) 2003 took place at the València Anchor Station (VAS, 39°33' N, 1°17' W), València, Spain, from day of year (DoY) 181 to 191, 2003. During the experiment period, the weather was very dry and warm, and in order to get a wide range of soil moisture values, the field was irrigated twice on DoY 182 and 185, and left to dry out. Concurrently with the radiometric measurements, the gravimetric soil moisture, the temperature and the roughness were measured, and the vines were fully characterized (water content, grapevine size, branch distributions, etc.) [5]. Radiometric measurements were acquired at incidence angles from 25° to 65° (Figure 7), and at azimuth angles from 45° to 135° with respect to the *X*-axis (or ± 45° with respect to the *Y*-axis, Figure 8). The antenna-to-target distance is defined as the distance between the sensor and the central point of the ellipse formed by the projected field-of-view over the soil. This distance was kept constant for both sweeps: elevation and azimuth.

The vines in this field are taller than others in the Mediterranean region, showing an average height of 1.63 m and width of 1.45 m (Figure 5a), and are planted on a 1.5 m × 2.5 m grid (Figure 5c; Table I of [5]). During the experiment, the measured volumetric water content was approximately 9-10 kg/m^2, from which 39.2% corresponded to the grapes, 31.5% to the stem, 10.5% to the primary branches, 2.5% to the secondary branches, 2.5% to the tertiary branches, and the rest to the leaves. The measured leaf area index (*LAI*) ranged from about 0.9 m^2/m^2 to 3.4 m^2/m^2.

Figure 7. Field-Of-View of the antenna footprints for incidence angles from 25° to 65° in 5° steps (azimuthal angle equal to 90°).

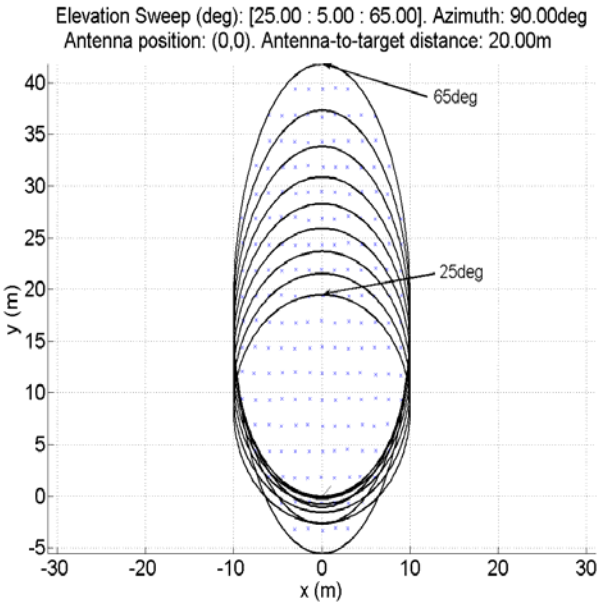

Figure 8. Field-Of-View of the antenna footprints for azimuthal angles from -45° to +45° in 15° steps (incidence angle equal to 45°).

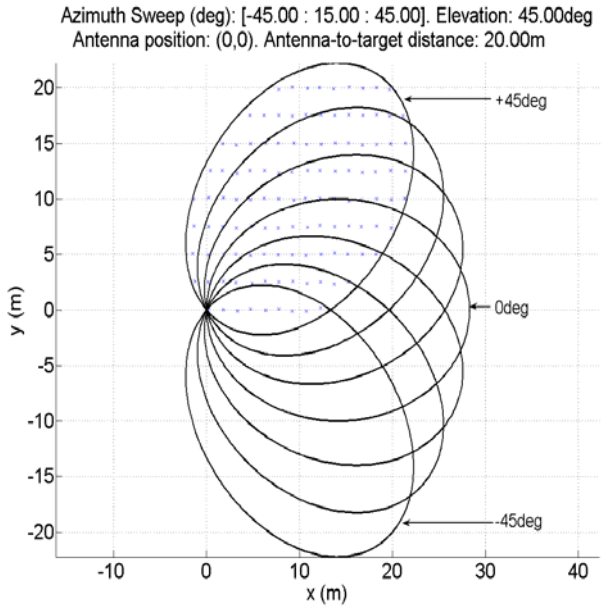

The plant has been modeled with 27 discrete branches and 195 stems, accounting for a volume of 5.58 and 0.79 dm^3, respectively, and a total surface area of 1.58 m^2 (Figure 5b). The number of leaves equivalent to an approximate *LAI* of 1.57 m^2/m^2 is 557, and they were modeled as flattened ellipsoids with semi-axes 6 cm and 5.5 cm, and 1 mm thickness. The volume occupied by the leaves is 5.77 dm^3, whereas the surface is 11.75 m^2. The grapes presented an average radius of ~1.1 cm, and the dry matter fraction was ~ 30%. The total number of grapes (791) is computed so that the volume water content (*VWC*) of the grapes corresponds to the measured one (39.2 % of the total *VWC* = 4.41 dm^3).

Figure 9. a) Computed albedo for the different components of the vegetation layer (fruits, stems, leaves and branches) and total single-scattering albedo (vegetation). b) Computed transmissivity for the different components of the vegetation layer (Fruits, Stems, Leaves and Branches) and total transmissivity coefficient (Vegetation).

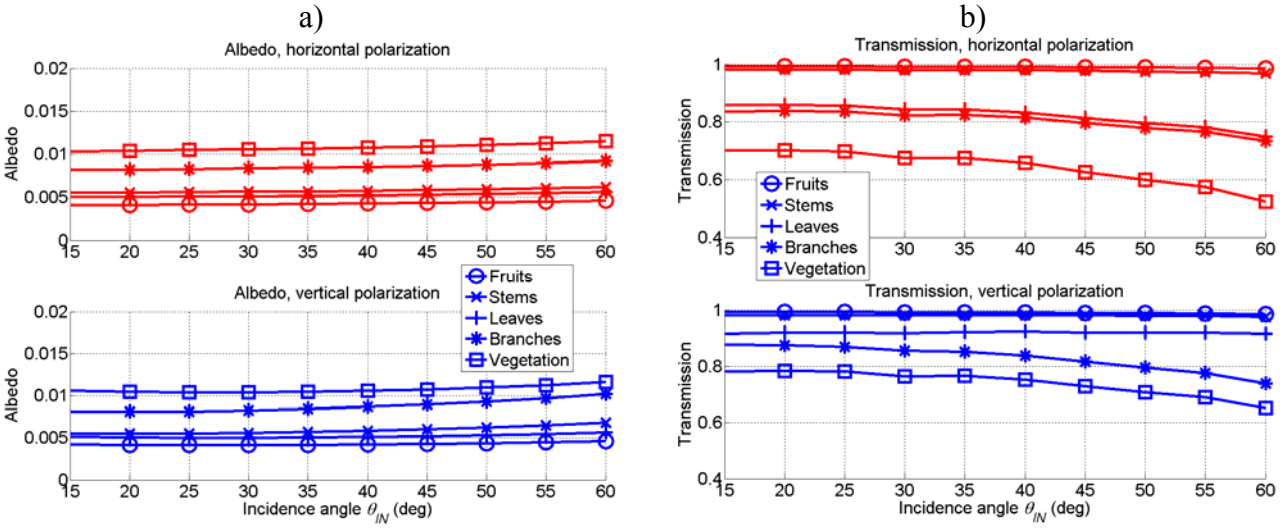

Figure 9a presents the computed single-scattering albedo of the vegetation layer and the individual contributions of the different components of the vegetation (fruits, stems, leaves and branches). The predicted albedo is very similar at both polarizations, it is mostly contributed by the branches, and it matches quite well the one obtained by fitting the radiometric measurements to the τ-ω model [Equation (1)], specially at high incidence angles (Figure 10a from [5]). However, the fitted albedo slightly decreases at higher incidence angle, whereas the simulated one is nearly constant or shows a minimal increase.

Figure 9b presents the total transmissivity of the vegetation as well as the contributions to the total transmissivity ($\Upsilon = e^{-\tau}$) of the different components of the vegetation layer separately in horizontal and vertical polarization. At vertical polarization. the predicted value at nadir agrees very well with the opacity (τ) fitted by adjusting the radiometric measurements to the τ-ω model (Figure 10b from [5]): at $\theta = 0°$, $\tau = 0.21$ and $\Upsilon = e^{-\tau} = 0.81$, and at $\theta = 55°$, $\tau = 0.61$ and $\Upsilon = e^{-\tau} = 0.54$. At high incidence angles ($\sim 55°$) the model seems to underestimate it, specially at vertical polarization where the predicted transmissivity is higher than the fitted one. However, it has to be recalled that, as pointed out in [5], the matching of the radiometric data to the τ-ω model usually employed at L-band was only possible for incidence angles smaller than 50°, in some cases at 55°, and never above 60°. Therefore, the inter-comparison of the predicted values has to be restricted to incidence angles smaller than 50°. As expected from the orientation and shape of the different vegetation parts, Figure 9b confirms that the main contribution to the extinction coefficient comes from both branches and leaves at horizontal polarization, and mainly from the branches at vertical polarization.

Figure 10. a) Albedo vs incidence angle. b) Opacity in Nepers vs incidence angle. Dots represent the retrieved value for each sequence and all azimuth angles, and line plots the mean value (Figure 8 from [5]).

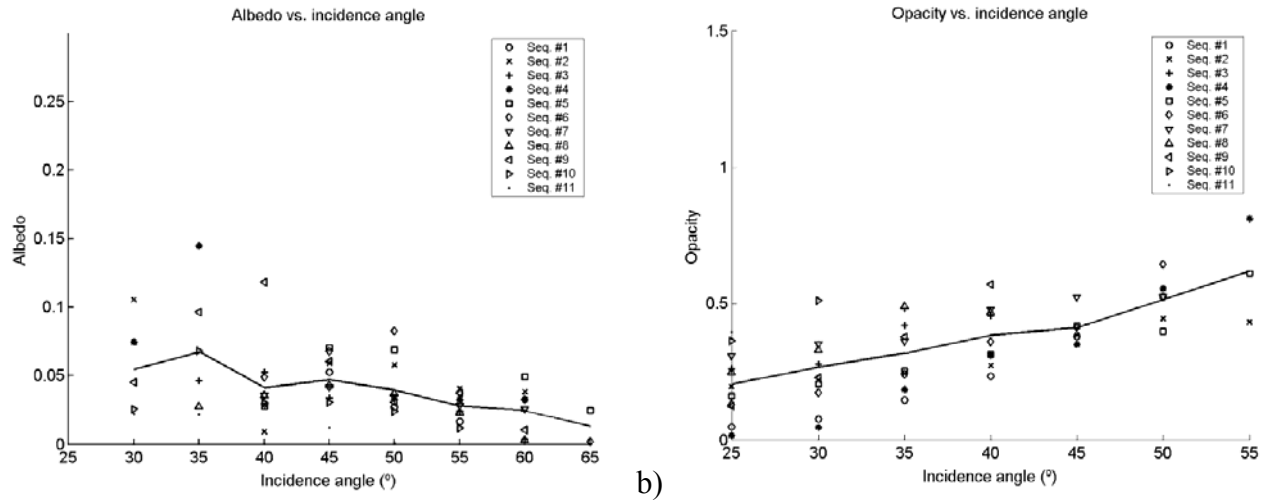

a) b)

Numerical experiments varying the size and *VWC* of the grapes predict only a variation of the single-scattering albedo with the scatterers' size, whereas the vegetation attenuation is nearly independent of the *VWC*. This confirms that in general the attenuation is dominated by the water content in the branches (and in the leaves at horizontal polarization), while grapes (and leaves at vertical polarization) exhibit mostly a scattering behavior [21].

Figure 11a shows the measured emissivities at horizontal and vertical polarizations for a wet (solid line) and a dry day (dashed line). Lines represent the mean value at each incidence angle for the scans at different azimuth angles (from -45° to 45°), and bars represent the associated geophysical fluctuations (rms values). Note that the fluctuations in DoY 185 (wet soil, solid line) are much higher than in DoY 181 (dry soil, dashed-dotted line), due to the variability of the soil moisture in the field, which was due to the gentle slopes and the presence of the vegetation (soil was wetter below the plants, and drier between them). Figure 11b shows the mean value (solid and dashed-dotted lines) and rms values (bars) of the emissivity as a function of the azimuth angle, averaged for all incidence angles for two representative days of experiment (wet day: DoY 185 solid line, and dry day: DoY 181, dash-dotted line). As it can be appreciated, the soil moisture content was slightly higher around azimuth ~0°, due to the gentle slopes of the terrain, which translates into a marked azimuthal signature, not attributable (at least to first order) to an azimuthal signature associated to the vegetation or the planting pattern. Again, in dry conditions, the azimuthal signature is negligible.

Figure 11. Emissivity at vertical and horizontal polarizations as a function of the incidence and azimuth angles. a) Mean value and standard deviation of the emissivity and of the ground-truth soil moisture as a function of the incidence angle and for all azimuth angles. DoY 185 (solid line) and DoY 181 (dashed-dotted line) have been represented. Blue and red indicate vertical and horizontal polarizations, respectively. b) Mean value and standard deviation of the emissivity as a function of the azimuth angle, for all incidence angles. Blue and red indicate vertical and horizontal polarizations, respectively. Values for two representative days of experiment have been represented: DoY 185 (solid line), and 181 (dash-dotted line). The averaged soil moisture at each observation position has been included (green lines).

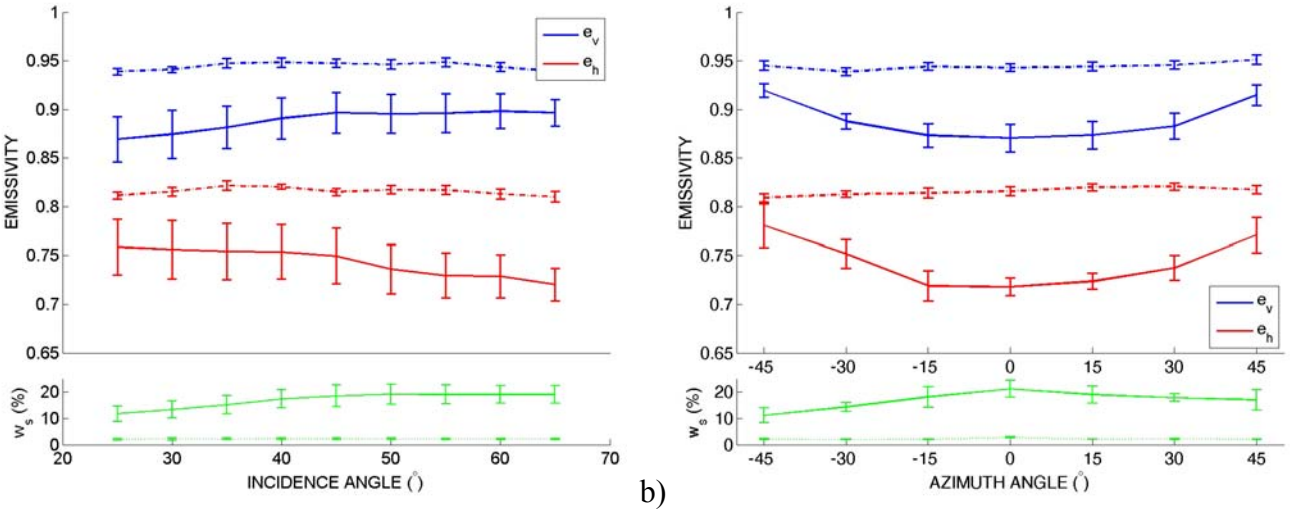

a) b)

The soil moisture variability complicates the intercomparison with numerical model predictions. Therefore, average values over the field have been taken, at the expense of larger error bars. Figure 12a shows the measured emissivities at horizontal and vertical polarizations for an average soil moisture of approximately 9%. Lines represent the mean value at each incidence angle for the scans at different azimuth angles (from -45° to 45°), and bars represent the associated geophysical fluctuations

(rms values). Figure 12b shows the bare soil emission computed using the τ- ω model (Section 2.1, dash-dot line) and the RTE for soil and vines (Section 2.2, solid line). As it can be appreciated, the agreement is relatively good at both polarizations, even though it seems to overestimate the emissivity, which is largely due to the lower predicted values for the single scattering albedo (ω in Figures 9a and 10a). This suggests that more complex and accurate models are still required for densely vegetated soils.

Figure 12. Emissivity at vertical and horizontal polarizations as a function of the incidence angle. a) Experimental data: mean value (solid line) and associated fluctuations due to different azimuth angles. b) Bare soil emission model from Section 2.2 (dashed line) and radiative transfer model computed from Equation (6) for soil and vines (solid line).

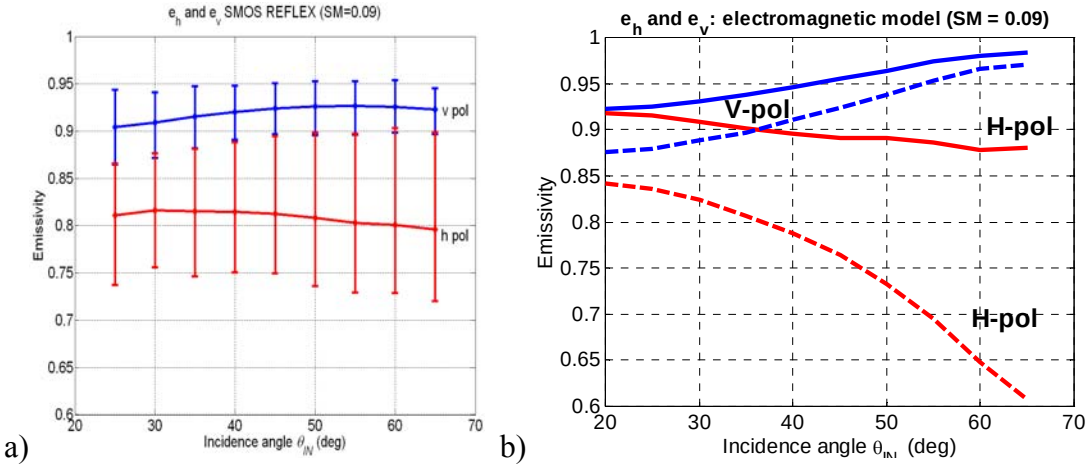

Figure 13 presents the third parameter of the Stokes modified emission vector (e_U) for the same vineyard as a function of the azimuth angle. The third and fourth Stokes elements are measured from the real and imaginary parts of the complex cross-correlation of the electric fields at vertical and horizontal polarizations as in Equation (1) [the third (fourth) Stokes parameter can also be measured as the difference between the brightness temperatures measured at two orthogonal linear (circular) polarizations at +45° and -45° (LHCP and RHCP)].

Solid lines correspond to the measured values in the field experiment, while the dashed lines are simulated values using Equation (6), scaled by a factor equal to 1/30. This empirical factor corresponds to the inverse of the approximate number of grapes per bunch, as if the whole bunch was a single scatterer and not an ensemble of smaller scatterers. While e_h and e_v are dominated by the scattering and attenuation in the branches, e_U seems to be dominated by the scattering in the bunches of grapes, and a clustering factor is needed to account for the random distribution of grapes used in the model (Section 4.3). Fluctuations in e_U are due to the planting pattern of the vineyard, and both the data and simulations show that e_U is nearly insensitive to soil moisture content.

Figure 13. Third parameter of the Stokes emission vector (e_U) as a function of the azimuth angle (incidence angle = 25, 45 and 65°): experimental data (solid lines) and radiative transfer model computed from Equation (6) (dashed lines) scaled by a clustering factor equal to 1/30 to account for near field effects between grapes. The fourth parameter (e_V) is equal to zero.

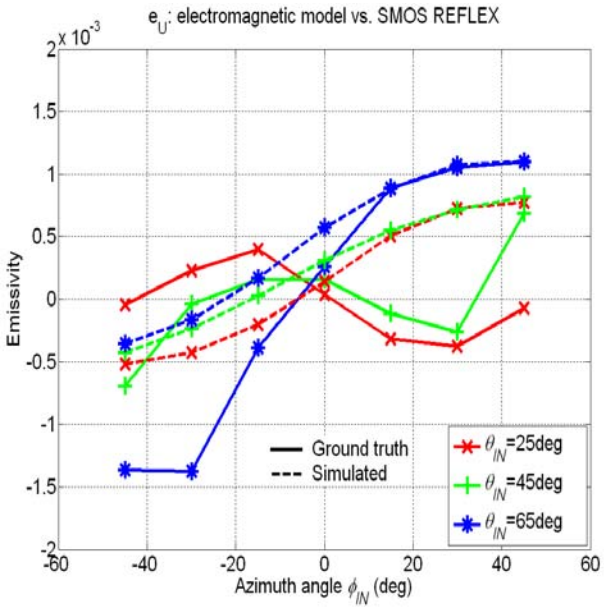

The magnitude of the measured and simulated fourth Stokes parameter (not shown) is negligible as there are no elements that induce a significant phase shift between the electric fields at horizontal and vertical polarizations.

6. Conclusions

This manuscript has described a complete modified Stokes emission numerical simulator of vegetation-covered soils and its application to the study of the influence of realistic L-systems generated vegetation and soil characteristics on the microwave emission at L-band. The four elements of the modified Stokes emission vector are efficiently computed by numerical integration of the scattering coefficients using analytical expressions for trunks and branches (dielectric cylinders), leaves (flattened dielectric ellipsoids), and grapes (lossy dielectric spheres). To keep the computation time reasonable, multiple scattering and clustering effects have been neglected.

As expected, it is found that the emissivity of the first two Stokes elements (e_h and e_v) is dominated by the soil moisture content, which impacts $\Gamma_{h,v}^{soil}$ through changes in the dielectric constant.

The impact of the vegetation layer on the total emissivity (albedo and attenuation) is dominated by the branch volume, whereas it is almost insensitive to the vegetation type and geometry, and the effect of the tree trunk and leaves is very small. The agreement between measurements and simulations is very satisfactory for the emissivity at vertical polarization. At horizontal polarization though, the simple soil emission models currently used prevent the combined soil + vegetation model to correctly follow the measured emissivity trend, since the bare soil emission model decreases too rapidly with

increasing incidence angles. Both the albedo and the vegetation attenuation, previously obtained by fitting the τ-ω model to the experimental data [5] agree well with the simulated values.

For a soil surface characterized by a zero-mean Gaussian slopes' pdf, the average emissivity of the third and fourth Stokes parameters is zero. However, for the vines scenario the predicted e_U is overestimated due to the random distribution of grapes used in the model, which neglects the clustering effects that take place in the bunches of grapes. A clustering factor roughly equal to the number of grapes per bunch must be included to adjust simulations and experimental data. On the other hand, within the measurement error level, e_V is zero, as confirmed by simulation results.

Acknowledgements

This work has been partially supported by the Spanish Comisión Interministerial de Ciencia y Tecnología and EU Feder (projects CICYT TEC2008-06764-C02, ESP2007-65667-C04-02 and AYA2008-05906-C02-01/ESP).

References and Notes

1. SMOS: ESA's Water Mission; BR-224; European Space Agency, June, 2004; p. 14, Available online: http://esamultimedia.esa.int/docs/br_224.pdf (accessed on 28 April, 2009).
2. Kerr, Y.H.; Waldteufel, P.; Wigneron, J.P.; Martinuzzi, J.; Font, J.; Berger, M. Soil moisture retrieval from space: the Soil Moisture and Ocean Salinity (SMOS) mission. *IEEE Trans. Geosci. Remot. Sen.* **2001**, *39*, 1729-1735.
3. Camps, A.; Vall-llossera, M.; Duffo, N.; Torres, F.; Corbella, I. Performance of sea surface salinity and soil moisture retrieval algorithms with different auxiliary datasets in 2-D L-band aperture synthesis interferometric radiometers. *IEEE Trans. Geosci. Remot. Sen.* **2005**, *43*, 1189-1200.
4. Berger, M.; Camps, A.; Font, J.; Kerr, Y.; Miller, J.; Johannessen, J.; Boutin, J.; Drinkwater, M.R.; Skou, N.; Floury, N.; Rast, M.; Rebhan, H.; Attema, E. ESA's activities for advancing the science underlying the ocean salinity objectives of the SMOS mission. *ESA Bull.* **2002**, No. 111, 113-121, Available online: http://esamultimedia.esa.int/docs/Cryosat/ESABulletin111-SMOSOSactivities.pdf (accessed on April 28th, 2009).
5. Vall-llossera, M.; Camps, A.; Corbella, I.; Torres, F.; Duffo, N.; Monerris, A.; Sabia, R.; Selva, D.; Antolín, C.; López-Baeza, E.; Ferrer, J.F.; Saleh, K. SMOS REFLEX 2003: L-band emissivity characterization of vineyards. *IEEE Trans. Geosci. Remot. Sen.* **2005**, *43*, 973-982.
6. Randa, J.; Lahtinen, J.; Camps, A.; Gasiewski, A.J.; Hallikainen, M.; Le Vine, D.M.; Martin-Neira, M.; Piepmeier, J.; Rosenkranz, P.W.; Ruf, C.S.; Shiue, J.; Skou, N. *Recommended Terminology for Microwave Radiometry*; NIST Technical Note TN1551; National Institute of Standards and Technology: Gaithersburg, MD, USA, August 2008; Available online: http://www.boulder.nist.gov/div818/81801/Noise/publications/TN1551.pdf (accessed April 28th, 2009).
7. Pardé, M.; Wigneron, J.P.; Chanzy, A.; Waldteufel, P.; Kerr, Y.; Huet, S. Retrieving surface soil moisture over a wheat field: Comparison of different methods. *Rem. Sens. Env.* **2003**, *87*, 334-344.

8. Tsang, L.; Kong, J.A.; Ding, K. *Scattering of Electromagnetic Waves, Theories and Applications*; Wiley-Interscience: New York, NY, USA, 2001.
9. Lin, Y.C.; Sarabandi, K. A monte carlo coherent scattering model for forest canopies using fractal-generated trees. *IEEE Trans. Geosci. Remot. Sen.* **1999**, *37*, 440-451.
10. Prusinkiewicz, P.; Lindenmayer, A. *The Algorithmic Beauty of Plants*; Springer-Verlag New York, Inc.: New York, NY, USA, 1990.
11. Martinez-Vazquez, A. *Emisividad Polarimétrica del Terreno: Efecto de la Vegetación*. Proyecto Final de Carrera. Advisor: Camps, A.; Escuela Técnica Superior de Ingeniería de Telecomunicación de Barcelona, Universitat Politècnica de Catalunya: Barcelona, Spain, 2001.
12. Martinez-Vazquez, A.; Camps, A.; Duffo, N.; Vall-llossera, M.; Lopez-Sanchez, J.M. Full Polarimetric Emissivity of Vegetation-Covered Soils: Vegetation Structure Effects. In *Proceedings of IEEE International Geoscience and Remote Sensing Symposium*, Toronto, Canada, June 24-28, 2002; Vol. 6, pp. 3542-3544.
13. Wang, J.R.; Choudhury, B. Remote sensing of soil moisture content over bare field at 1.4 GHz frequency. *J. Geoph. Res.* **1981**, *86*, 5277-5282.
14. Wang, J.R. The dielectric properties of soil water mixtures at microwave frequencies. *Radio Sci.* **1980**, *15*, 970-985.
15. Wang, J.R.; Schmugge, T.J. An empirical model for the complex dielectric permittivity of soils as a function of water content. *IEEE Trans. Geosci. Remot. Sen*. **1980**, *18*, 288-295.
16. Dobson, M.C.; Ulaby, F.T.; Hallikainen, M.T.; El-Rayes, M.A. Microwave dielectric behaviour of wet soils, Part II: dielectric mixing models. *IEEE Trans. Geosci. Remot. Sen*. **1985**, *23*, 35-46.
17. Ulaby, F.T.; Elachi, C. *Radar Polarimetry for Geoscience Applications*; Artech House: Norwood, MA, USA, 1990.
18. Lin, Y.C.; Sarabandi, K. Electromagnetic scattering model for a tree trunk above a tilted ground plane. *IEEE Trans. Geosci. Remot. Sen.* **1995**, *33*, 1063-1070.
19. Ishimaru, A. *Electromagnetic Wave Propagation, Radiation, and Scattering*, 1st ed.; Prentice Hall: Englewood Cliffs, NJ, USA, 1991; pp. 290-294.
20. Karam, M.A.; Fung, A.K.; Antar, Y.M.M. Electromagnetic wave scattering from some vegetation samples. *IEEE Trans. Geosci. Remot. Sen.* **1988**, *26*, 799-808.
21. Ferrazzoli, P.; Guerriero, L.; Wigneron, J.P. Simulating L-band emission of forests in view of future satellite applications. *IEEE Trans. Geosci. Remot. Sen.* **2002**, *40*, 2700-2708.